Production and transport of long-lifetime excited states in preequilibrium ion-solid collisions

Emily Lamour*
INSP, CNRS UMR 75-88, Universités P. et M. Curie and D. Diderot, 140 rue de Lourmel, 75015 Paris, France

Benoît Gervais
CIRIL, UMR 6637 CEA-CNRS-ENSICAEN, Boîte Postale 5133, 14070 Caen Cedex 5, France

Jean Pierre Rozet and Dominique Vernhet
INSP, CNRS UMR 75-88, Universités P. et M. Curie and D. Diderot, 140 rue de Lourmel, 75015 Paris, France
(Received 7 February 2006; published 21 April 2006)

A complete experimental study of the production and transport of long-lifetime excited states has been done for Ar^{18+} on solid C targets, at a velocity of 23 a.u., and for a range of thickness allowing us to vary the transport conditions from single collision to equilibrium (3.5 to 201 $\mu g/cm^2$). A systematic determination of Ar^{17+} Rydberg ℓ- and $2s$-state populations has been performed using the x-ray spectroscopy technique. Results are compared with predictions of different transport simulations (developed on either a quantum or a classical phase space), which take into account multiple collisions and the strong polarization induced by the incoming ion (the wakefield). Using the continuum distorted-wave approximation for modeling the initial capture process, very good agreement is found between experimental Rydberg-state populations and theoretical approaches limited to the effect of multiple collisions. On the contrary, the transport of the metastable $2s$ state exhibits strong sensitivity to Stark mixing induced by the wakefield. The limitation of each theoretical approach is discussed with respect to the different experimental observables.

DOI: 10.1103/PhysRevA.73.042715 PACS number(s): 34.50.Fa, 39.30.+w, 34.10.+x

I. INTRODUCTION

Research on ion-matter interaction covers a large domain from the study of elementary physical processes involved in ion-atom collisions to the radiation damage in inert or biological materials. In addition to some fundamental aspects, atomic collision studies are useful to understand the effects associated with energy deposition in matter [1]. In this frame, transport of electrons in excited states of fast ions through solids is a subject of current investigation. Indeed, a single electron bound to a nucleus allows one to achieve experimentally a simply tunable system to probe directly the ion-solid interaction by a proper choice of the ion velocity v_P and the atomic number Z_P. Two specific effects of solid media have been evidenced: the enhanced production of Rydberg states when compared to single ion-atom collisions, and the mixing of the internal states of the projectile by the wakefield induced by the large charge of the projectile nucleus. So far, however, the production and transport of inner-shell and Rydberg projectile states were determined through experiments performed separately and the behavior of the state populations with respect to different transport processes was interpreted in each case by different theoretical approaches. This led to controversial interpretation of the transport effects of projectile electrons.

On the one hand, several authors observed high-ℓ populations in Rydberg states. In their last studies, Betz and collaborators [2,3] demonstrated that Coulomb capture of target electrons from the last layer of atoms in the solid (just when the ion exits into vacuum) could not explain the observed ℓ populations of Rydberg states. Provided the target is thin enough to avoid equilibrium in the state population, they showed that Rydberg states of fast ions are not formed predominantly by direct capture of target electrons. They found, instead, a connection between projectile core electrons and final Rydberg states. They invoked here a strong contribution of ionized electrons (over all bound projectile electrons), which have large probabilities to undergo transitions into Rydberg states. On the contrary, results of ℓ-Rydberg-state populations (O^{2+} (v_p=9 a.u.) on C, 20 $\mu g/cm^2$ [4,5]) have been interpreted as transport of projectile electrons with a classical Monte Carlo simulation taking into account properly multiple scattering effects. This classical model, pioneered by Burgdörfer and collaborators [6,7], describes the motion of the projectile electron on a classical orbit perturbed by a stochastic force chosen to represent multiple scattering by the surrounding medium. However, in that case, the understanding of the projectile electron transport was far from complete: (i) the target was thick enough to reach equilibrium for the charge-state distribution and (ii) capture of the target electron and excitation or ionization of the $1s$ projectile initial state are of the same order of magnitude. Thus, different processes are involved in the "primary" production of excited states and the division between the "initial" excited-state population and transport effects cannot be determined.

On the other hand, for inner-shell populations, extensive studies have been performed on the charge-state distribution, on np populations, as well as on the fine-structure substate ($n\ell_j$) populations for several collisional systems [8]. A range of target thickness from single-collision conditions to equi-

*Corresponding author. Electronic address: emily.lamour@insp.jussieu.fr

librium has been investigated. Different theoretical approaches have been developed and applied to explain the transport of core projectile excited states, which exhibit different degrees of sensitivity to various processes experienced by the projectile electron in the solid; namely, transport simulations account for multiple collisions, the strong target polarization induced by the incoming ion (the wakefield), and the radiative decay inside the foil when it competes. Theoretical work has been carried out to determine the population of a given state at the exit of the foil. They are all based on the Liouville equation to describe the dynamical evolution of the ion during the interaction, with various degrees of approximations, classically or quantum mechanically. The Liouville equation is solved either directly as a matrix equation (the so-called master-equation approach [9,10]) or by Monte Carlo simulations [9,11–14]. From a comparison with experiments, one can draw up an overview of the main results. The evolution of charge-state distributions, involving only core-state populations, is well reproduced by a model based on master equations taking into account only collisional processes (i.e. the rate-equation model [15]). On the contrary, the collisional approach cannot explain alone the experimental data concerning transport of $n\ell$ inner shells through solid foils. The combined effect of the wakefield induced by the ion in the solid and multiple collisions has been found to play a major role in explaining the evolution of np inner-shell populations with target thickness for different collisional systems; namely, Ar^{18+} at $v_p=23$ a.u. on C [12,16]; Kr^{36+} at $v_p=35$ a.u. on C and Cu [17,18]; Kr^{35+} at $v_p=47$ a.u. on C and Al [9,12,14,19]. Furthermore, the behavior of the $3\ell_j$ populations of Kr^{35+} (for all cases mentioned above), as a function of ion transit time through the solid, has demonstrated very strong sensitivity to the effective value of the wakefield. It even exhibits remaining oscillations of the induced Stark mixing between substates.

In this paper, we present an experiment where both Rydberg- and core excited-state populations of 23 a.u. Ar^{17+} ions after transmission through thin carbon foils have been measured. We focus on the presentation of long-lifetime excited states, i.e., Rydberg and $2s$ states. A complete analysis has been made over a wide range of target thickness (from 3.5 to 201 $\mu g/cm^2$) in order to vary extensively the number of collisions the projectile electron suffers in the solid (from $\approx$0.6 to 60 collisions). Moreover, absolute cross sections have been determined for x-ray emission from the Rydberg states and for the population of the $2s$ state. Great care was taken in the choice of the collisional system. Indeed, decisive questions remain: one concerns generally the effect of transport on the population of Rydberg states; the other is relevant to the sensitivity of the population of long-lifetime states to the wakefield during the transport. Therefore the system has been chosen to allow tests of transport effects satisfying the following criteria. First, using incoming Ar^{18+} ions, the primary production process of excited states—single capture—is well identified and multiple-capture probabilities through successive collisions can be neglected even for the thickest target (probability $\leqslant$3%). Second, the transport of the initial excited states is mainly due to excitation and ionization processes. Finally, a classical description of the Ar n level is still valid down to quite low n values [5] and radiative decay inside the target itself can be neglected (only $\approx$4% of excited states—mainly the $2p$ state—decay inside the thickest carbon target). This last remark suggests that a comparison of experimental data to classical approaches might be meaningful even for the inner shells. Therefore as already discussed for the np states [12], quantum and classical transport theories can be applied as well for this particular system.

TABLE I. Respective contributions of direct and cascade populations to the total population for different $n\ell$ states and two target thicknesses. The direct contribution corresponds to the population at the exit of the foil. The cascade contribution corresponds to the population coming from upper levels by radiative decay behind the foil.

	3.5 $\mu g/cm^2$ target		98 $\mu g/cm^2$ target	
$n\ell$ state	% direct	% cascade	% direct	% cascade
$2p$	60	40	51	49
$2s$	74	26	84	16
$3p$	89	11	86	14
$4p$	$\approx$100		99	1

In the following, the paper is organized in three principal parts. In Sec. II, we give a complete description of the experiment and we detail the results analysis. The different theoretical approaches are summarized in Sec. III, followed by a discussion on the comparison with the experimental data in Sec. IV. The experimental precision reached allows us to shed light on the validity limits of the various theoretical approximations of transport effects without the wakefield (collisional models) or with the wakefield included. Conclusions and perspectives are reviewed in the last section.

II. EXPERIMENT

Keeping in mind that lifetimes of hydrogenlike $n\ell$ states are proportional to $n^3\ell^2$ for a given projectile, the delayed photon emission observed in the decay of $2p$ and $3p$ states (which have very short lifetimes, i.e., 1.52×10^{-14} s for $2p$ and 5.12×10^{-14} s for $3p$) comes from the Rydberg-state population through the cascade contribution. Therefore, the observation of the Lyman ($np\rightarrow1s$) line intensities as a function of the ion time of flight behind the target for several thickness is a direct signature of high-angular-momentum Rydberg-state populations [2–4,20,21]. For reference, the respective contributions of direct and cascade populations of a given np state just at the exit of the foil are specified in Table I. These contributions have been estimated through the theoretical approaches described in Sec. III. Whatever the approach used, contributions of cascades on np states are of the same order within 10%. Obviously, if instead of looking just at the exit of the foil, the Lyman line intensities are recorded at a given ion time of flight behind the target, the cascade contribution becomes larger. Beam-foil spectroscopy also allows one to get information on the population of the $2s$ meta-

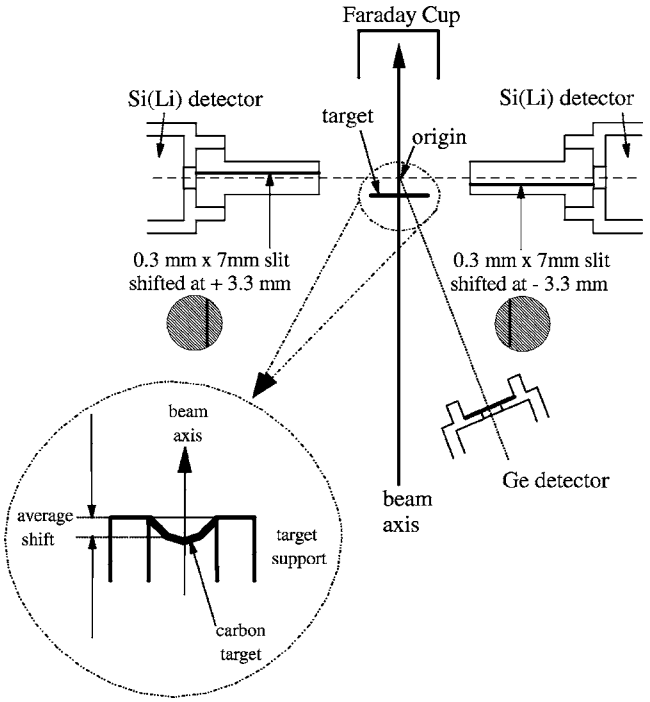

FIG. 1. Schematic representation of the experimental setup. Effects leading to x-ray autoabsorption are displayed in a zoom (see text).

stable excited state. This gives, here for the $2s$ state, a direct insight into the evolution of an inner-shell population during ion-solid interaction since the cascade contribution is small (Table I). We have thus studied the evolution of the $2s \rightarrow 1s$ emission with target thickness, i.e., the transit time of ions inside the solid. In the following, we detail experimental aspects since in this work absolute cross sections have been extracted.

A. Experimental setup

The experiment has been performed on the Sortie Moyenne Energie (SME) facility at Grand Accélérateur National d'Ions Lourds (GANIL), Caen, France. The experimental setup is schematically depicted in Fig. 1. A beam of 13.6 MeV/u Ar^{18+} ions is directed onto thin carbon foils which can be accurately translated along the beam axis.

The delayed ($np \rightarrow 1s$) x rays emitted by the projectile are analyzed at 90° with respect to the beam direction at different distances behind the foil by two Si(Li) detectors. Energies of the Ar^{17+} Lyman lines are given in Table II. The Si(Li) detectors are placed on the opposite side of the beam, facing each other. Decay lengths (along the beam axis) in the effective range from 0 to 50 mm, corresponding to delay times up to 1 ns, are explored with a 6 ps time resolution. To ensure this resolution a collimation system using slits of 60.4 mm long, 0.3 mm wide, and 7 mm high is placed in front of each Si(Li) detector. In order to record two different spectra during a given acquisition time, each slit is shifted with respect to the center of the collision chamber (i.e., beam axis origin) by either +3.3 or −3.3 mm (see Fig. 1). Overlap measurements are also ensured at a given distance from the foil by the two Si(Li) detectors. Despite the precision of the stepping motor used for target translation along the beam axis (1 μm), the "0" position has been scanned for each foil to control the specific shadow effects entailed by the target supports as well as the x-ray autoabsorption, which depends upon the target flatness (see zoom in Fig. 1). These two different effects are important and have to be taken into account when comparing absolute experimental values with theoretical predictions (see Sec. III C).

TABLE II. Energy of each observed line with the associated efficiency and global transmission for one of the Si(Li) detectors. The efficiency of the other Si(Li) detector corresponds to 70% of the values given here. E_{proj} and E_{lab} correspond, respectively, to energies in the projectile and laboratory frames. Energies of the Lyman line are taken from Ref [23]. The asterisk marks the energy of the center of the theoretical distribution of the $2E1$ decay mode [22].

	Energy (eV)		Si(Li) detector	
Observed lines	E_{proj}	E_{lab} (θ_L=90°)	Efficiency	$T^{n\ell}_{glob}$
Ly-α	3321	3273	0.83 (±7%)	8.62×10^{-6} (±9.5%)
Ly-β	3936	3879	0.88 (±7%)	9.20×10^{-6} (±9.5%)
Ly-γ	4150	4091	0.90 (±7%)	9.36×10^{-6} (±9.5%)
Σ_5^∞ ($np \rightarrow 1s$)	4362	4299	0.91 (±7%)	9.50×10^{-6} (±9.5%)
$2E1$	1660*	1636*	0.39 (±8%)	4.01×10^{-6} (±10.5%)

In addition, a Ge detector placed at 150° with respect to the beam axis recorded all the emitted x rays with the target located at the center of the collision chamber. This has allowed us to determine, for each target thickness, the cross section of Lyman line production mainly due to "prompt" emission as presented and discussed previously [12].

Beam intensity (in the 10–500 nA e range) is measured by a Faraday cup with a typical precision better than 1%. Seven self-supported carbon foils of thickness ranging from 3.5(±27%) to 201(±5%) μg/cm^2 have been used. The thickness as well as the impurity content are measured by means of Rutherford-backscattering analysis with 2 MeV α particles produced by a Van de Graaff accelerator. We have selected targets where impurities contribute less than 15% to the total capture signal. The most frequent impurity is oxygen, with a relative content varying between 0.3% and 5%.

B. Detection

The intrinsic energy resolution of each Si(Li) detector used is found to be around 7% corresponding to linewidths of ≈230 eV at 3.273 keV. This allows us to identify Ar^{17+} Ly-α ($2p \rightarrow 1s$), Ly-β ($3p \rightarrow 1s$), Ly-γ ($4p \rightarrow 1s$), and the sum of the remaining Lyman lines, i.e., $\Sigma_5^\infty(np \rightarrow 1s)$, as well as the $2E1$ decay mode of the $2s$ metastable state since its energy distribution is centered on 1.636 keV (theoretical value), well below the Ly-α line. As is well known, the $2s$ metastable state (with a lifetime of 3.5×10^{-9} s for Ar^{17+}) has two decay modes: a two-photon mode ($2E1$) and a

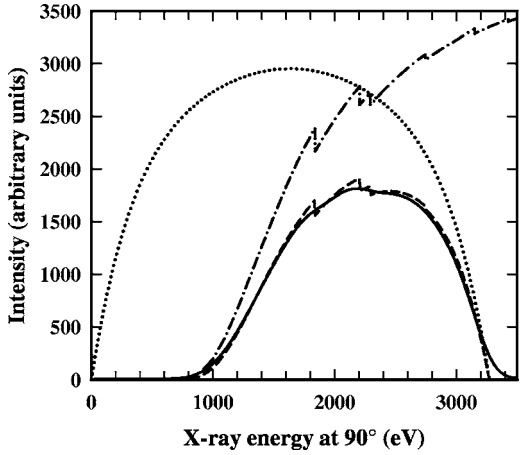

FIG. 2. Energy distribution of the $2E1$ decay mode for an Ar^{17+} ion: the theoretical distribution (dotted line), the distribution corrected by the Si(Li) detector efficiency alone (dashed line), and the "experimental" distribution (solid line), i.e., the distribution corrected by the efficiency convoluted with the detector resolution. Si(Li) detector efficiency is also plotted (dash-dotted line) for sake of clarity.

single-photon magnetic mode ($M1$) with branching ratios respectively of 97% and 3% in that case [22,23]. But, with Si(Li) detectors, it is obviously not possible to separate the two fine-structure components of the Ly-α line ($2p_{1/2}-2p_{3/2}=4.81$ eV) and even less the $M1$ transition from the $2p \rightarrow 1s$ one (the Lamb shift $2p_{1/2}-2s_{1/2}=0.158$ eV [23]). Thus, the extraction of the $2E1$ photon intensity, with a good accuracy, is imperative for both purposes. One is to determine the evolution of the $2s$ population with the target thickness (one task presented here). The other is to correctly subtract the $M1$ line contribution to the observed Lyman α' (Lyman α'=Lyman $\alpha+M1$) emission and to determine the "pure" $2p$-state population, especially for large ion times of flight where the contribution of the $2s$ decay becomes important.

The use of Si(Li) at these low x-ray energies requires a detailed study of the efficiency and of the response function connected to the energy resolution together with a precise determination of the solid angle, in order to obtain meaningful absolute values of cross sections. Specific studies of the detection efficiency and the response function have been performed with different calibrated radioactive sources providing a large variety of x-ray lines over a wide range of energy. The efficiency for each Lyman line is given Table II. The collimators in front of each detector define a geometrical solid angle, which leads to a global transmission $T^{n\ell}_{glob}$ reported in Table II. For the $2E1$ decay mode, we determine the mean efficiency by the ratio between the integrals of the "experimental" and the well-known theoretical energy distribution [22] of this two-photon decay mode. The experimental energy distribution is obtained, as illustrated in Fig. 2, by taking into account the efficiency and the intrinsic resolution responses of a Si(Li) detector. This permits one to go beyond an efficiency value and to get a complete knowledge of the experimental shape of the observed $2E1$ decay mode, which is of importance for the data analysis as discussed in the following section.

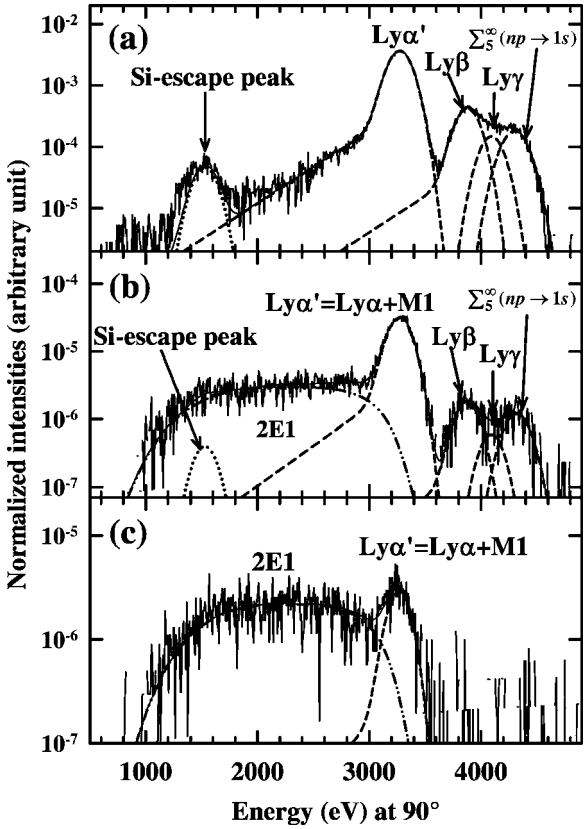

FIG. 3. Spectra recorded by a Si(Li) detector with sources of background subtracted at various ion times of flight (delay times) behind the 3.5 $\mu g/cm^2$ carbon target: t=(a) 0; (b) 108 ps; (c) 600 ps.

C. Spectral analysis and extraction of experimental data

108 spectra recorded by the Si(Li) detectors have been analyzed. We present Fig. 3 as an example, three spectra recorded by one of the Si(Li) detectors at various delay times t and for a given carbon target thickness (3.5 $\mu g/cm^2$). We can distinguish the set of the different Lyman lines described above and the $2E1$ photon emission. The Ly-α' line decreases less rapidly with t than the other Lyman lines for two reasons. One is related to the fact that the $2p$ state is more populated by very high-$n\ell$ excited states (i.e., of long lifetime) through cascades than are np states with $n \geqslant 3$. The second comes from the increased fraction of $M1$ in the Ly-α' line for large delay.

Spectra like those presented in Fig. 3 have been analyzed after subtraction of background, which has different behaviors depending on t. For t less than 9 ps, the background has mainly two components. The first one is due to the well-known bremsstrahlung process that has been simulated using estimated cross sections [24–26] and taking into account the efficiency and the intrinsic resolution of detectors. The contribution of this component to the signal remains reasonably small. We found, for instance, a maximum contribution less than 1% for the Ly-α' line and 2.5% for the Ly-γ line. The second background source comes from the interaction of the ion beam with the target holder. To get an accurate estimation of its contribution, we have recorded spectra with the

ion beam passing through a holder without carbon foil. For $t<9$ ps, this contribution does not go beyond 0.5% for the less intense line (Ly-γ line). For $t>9$ ps, only this background remains. It becomes critical when the signal-to-background ratio decreases (i.e., for large ion time of flight). For instance, at $t=198$ ps, we got 35% of the background contribution under the Ly-γ line.

With sources of background subtracted, a complete knowledge of the x-ray line shapes is needed to determine the line intensities. The shape of the recorded $2E1$ decay mode has been explained above (see Fig. 2), but Lyman peak shapes depend also on the response function of Si(Li) detectors. In the 1–6 keV energy range, this response consists of a dominating Gaussian peak, a low-energy tail, and a steplike function term [27,28]. A clear physical mechanism to explain this last term is not really yet known. Nevertheless, incomplete charge collection effects due to the dead layer of Si(Li) detectors explain the origin of the low-energy exponential tail. A left exponential function with a constant width was used to simulate this tail. Its proportion with respect to the principal peak depends on experimental conditions and more particularly on counting rates, which were kept almost constant during the experiment. We find a proportion of 15% for the Ly-α' and Ly-β lines. A precise determination of this low-energy tail is required to extract an accurate $2E1$ intensity, especially for short ion times of flight. The knowledge of all these line shapes allows us to decompose spectra as illustrated in Fig. 3. Knowing the counting rate of the $2E1$ transition, N^{2E1},N^{M1} are extracted using the well-known branching ratios, and from there, $N^{\text{Ly-}\alpha}$ of the "pure" Ly-α line is deduced. The contribution of the $M1$ deexcitation mode to the Ly-α' can be large. For example, a contribution from 10% for the 201 μg/cm^2 target up to 20% for the 3.5 μg/cm^2 target is reached for a delay time of 788 ps.

All the characteristics described above allow one to obtain reliable emission intensities values, $I_{n\ell\rightarrow 1s}$. On the one hand, information on the Rydberg ℓ-state population is related to the evolution of the number of emitted photons per ion for a given $np\rightarrow 1s$ transition ($\tilde{N}^{np}_{X/ion}$) as a function of the distance behind the solid target. For a certain distance, $\tilde{N}^{np}_{X/ion}$ is determined using the following equation:

$$\tilde{N}^{np}_{X/ion}=\frac{I_{np\rightarrow 1s}}{N_{proj}T^{n\ell}_{glob}}, \tag{1}$$

where N_{proj} stands for the number of projectiles and $T^{n\ell}_{glob}$ for the global transmission.

On the other hand, the absolute values of the $2s$-state population per incident ion have been obtained from a spectrum recorded at a given distance d behind the target, using the following relation:

$$P_{2s/ion}=\frac{I_{2E1}(d)}{2R^{2E1}_{2s\rightarrow 1s}N_{proj}T^{n\ell}_{glob}}\left\{\exp\left(\frac{-d}{\lambda}\right)\left[1-\exp\left(\frac{-L}{\lambda}\right)\right]\right\}^{-1} \tag{2}$$

where $R^{2E1}_{2s\rightarrow 1s}$ is the branching ratio, λ the metastable $2s$ radiative decay length (173.6 mm for Ar^{17+} at $v_p=23$ a.u.), and L the effective interception length (equal to 0.62 mm, equivalent to a resolution time of 6 ps).

III. THEORETICAL APPROACHES FOR TRANSPORT DESCRIPTION

The choice of the collisional system (Ar^{18+} at $v_p=23$ a.u. on C foils) allows us to apply a classical simulation of projectile electron trajectories even for inner shells (see Sec. I). Therefore, we can confront all the experimental results (Rydberg and inner-shell populations) with two kinds of treatment—classical and quantum—to interpret effects due to transport of hydrogenlike ions. We used and made specific improvements of the master-equation approach as well as of the classical Monte Carlo method. The main hypotheses of these different approaches have been given elsewhere [8,10,12]. For that reason, we focus on the modifications and the specific treatments brought to these models in order to achieve comparison with the experimental data presented in this paper, in particular for the Rydberg states.

Prior to transport, one electron of the carbon foil is captured by the Ar^{18+} ion. This primary process is accounted for by using the continuum distorted-wave [29,30] (CDW) approximation, being aware of some limitations in this choice [9]. Let us note that, the capture process enters as a constant term through the target in the different calculations presented below. This approximation implies that we regard the source term as independent of the projectile population, which leads to an overestimation limited to 4% of the $2p$ state population for the thickest target (the worst case).

A. Master- and rate-equation approach

To describe the transport of hydrogenlike projectile excited states, we use, on the one hand, the master-equation approach [10,19] to solve the quantum Liouville equation, which governs the time evolution of the projectile electron. This equation contains dissipative and nondissipative terms. Dissipative terms illustrate the interaction with the environment and include multiple collisions and radiative decay, while nondissipative terms describe the free time evolution of the electron in the screened Coulomb potential of the ion (i.e., the wakefield effect). This quantum approach allows us to follow the evolution of populations of each $n\ell_j m_j$ state and thus coherences between states. All the substates of the $n=1-6$ shells are included in the treatment. Actually, convergence for calculations is reached around $n=6$ (changes when going from $n_{max}=5$ to 6 do not exceed 2% for the studied observable). The number of atomic cross sections one should calculate for capture, ionization, intrashell and intershell excitation processes (i.e., 4195 cross sections), and coherence terms (i.e., 245 terms) give indeed a limitation to this type of treatment. Therefore, the master-equation approach is very suitable to interpret the inner-shell populations, in particular for np states up to $n=4$ and for $2s$. For the Rydberg-state populations, where higher n values have to be considered, we have simplified the master equations to rate equations. In fact, neglecting the wakefield effect, i.e., taking into account only the collisional processes and the radiative

decay, the $n\ell_j m_j$ basis can be reduced to the $n\ell$ basis. In practice, additional $n\ell$ states can be thus easily introduced in the treatment. At the present time, the treatment involving all the cross sections of collisional processes [i.e., radiative decay, capture, ionization, intra- ($\Delta n=0$) and intershell ($\Delta n=\pm 1$) excitation] is complete up to $n=10$. We have already demonstrated that the experimental delayed Lyman intensities for Ar^{17+} ions are, in fact, sensitive to all the excited states up to $n=30$ even if only 3% of excited states have a principal quantum number $n>10$ [16]. Hence, in order to overcome this intrinsic limitation, we assume an n^{-3} law [31] for states with $n>10$. The predictions of this rate-equation model neglecting the wakefield effect will be compared to the observed Rydberg-state populations in Secs. IV A and IV B. The master-equation approach will be compared with the evolution of the $2s$ state with target thickness (Sec. IV C).

B. Classical Monte Carlo methods

On the other hand, we simulate the transport of the projectile electron with a classical Monte Carlo method [7]. The use of a classical phase space is very suitable to interpret the Rydberg-state populations since no limitation in the number of states involved has to be considered. In the present paper, we have especially studied within this approach, the influence of the wakefield on ion transport. Indeed, this effect was found to have an important role in the evolution of prompt Lyman intensities as a function of target thickness due to its interplay with multiple scattering [12]. It was also shown that the dynamics of Rydberg states in the wakefield is chaotic [32], which leads to a considerable enhancement of the "loss of population" (the so-called "cutoff"). For the system under consideration, this cutoff is excepted to occur for states above $n\approx 15$ and therefore, one should check the sensitivity of the delayed Lyman intensity to the wakefield. The inclusion of the wakefield in the calculation is technically a challenge. The numerical integration of electron trajectories is computationally much slower than for the pure Coulomb case. It is therefore difficult to achieve a meaningful statistical accuracy of photon intensity for long delay. Previous calculations [12] made use of an approximated uniform wakefield, dependent on the Coulomb electron orbital energy, obtained from a dielectric response function based on local density approximation [9,33], but including only valence electrons. In order to have a consistent calculation with the ion slowing down involving also core electrons, we apply the Ashley dielectric function including carbon $1s$ excitation for both the collisional kernel and the wakefield calculation. For electron-nucleus vectors $\boldsymbol{r}$ such that r is smaller than 10 a.u., we use the expansion of Legendre polynomials $V_{wake}(\boldsymbol{r})=\Sigma_{k=0}^{50} V_k(r)P_k(\cos\theta)$, where P_k is the Legendre polynomial of degree k and θ is the angle with respect to the beam axis. For larger radii we employ a direct numerical integration with fast Fourier transform, which is more precise at larger distance but rather inaccurate at small r. To speed up the calculation, we exploit the secular approximation, which gives the evolution of the angular momentum $\boldsymbol{L}$ and the Lenz vector $\boldsymbol{A}$. We restrict its use for orbital energy E lower than $E=-18$ a.u., i.e., for orbits such as $r<1$ a.u.. For these low-energy orbits, we confine the spherical harmonic expansion to $\ell=0$, 1, and 2. We check that the Stark period is reproduced within 10% depending on the orbit orientation with respect to the projectile velocity v_p. When averaged over several orientations, the Stark period is reproduced within a few percent. From only $\boldsymbol{L}$ and $\boldsymbol{A}$, the orbit shape evolution can be defined but not the electron position. This information is, however, of minor importance for our purpose, and a new electron position is obtained by randomly choosing a new eccentric anomaly in a uniform distribution. In the following, the predictions of the classical approach with and without the wakefield (wake "on" and wake "off") are compared with the various experimental data on core and Rydberg-state populations.

C. Inclusion of cascades and instrumental response

The models and the simulation of the post foil interaction cascade processes lead to the number of emitted photons per ion and per time unit for an $n\ell\rightarrow 1s$ transition:

$$\frac{dN_{X/ion}^{n\ell}(t)}{dt}=A_{n\ell}^{1s}U_{n\ell}(t), \tag{3}$$

where $U_{n\ell}(t)$ is the fraction of ions with one electron in a $n\ell$ state and $A_{n\ell}^{1s}=\Sigma_{n',\ell'}A_{n\ell}^{n'\ell'}$ the $n\ell\rightarrow 1s$ transition probability per time unit. To compare with experiment, we have to keep in mind that the observed intensity $\tilde{N}_{X/ion}^{n\ell}(t)$ is integrated over the time interval determined by the width of the collimator placed in front of the Si(Li) detectors. $\tilde{N}_{X/ion}^{n\ell}(t)$ is then given by

$$\tilde{N}_{X/ion}^{n\ell}(t)=\int_Z \frac{dN_{X/ion}^{n\ell}(Z+\Delta)}{dZ}\varepsilon_g(Z)dZ, \tag{4}$$

$$\text{with } \frac{dN_{X/ion}^{n\ell}(Z)}{dZ}=\frac{1}{v_p}\frac{dN_{X/ion}^{n\ell}(t)}{dt} \tag{5}$$

Z is the position where $n\ell$ to $1s$ transitions are recorded. The average shift Δ accounts for the x-ray autoabsorption due to the target itself, the target holder and eventually the target curvature. The geometrical efficiency function $\varepsilon_g(Z)$, accounting for specific shadow effects entailed by the target holders, is detailed in the Appendix.

IV. RESULTS AND DICUSSION

A. Rydberg-state populations

1. Relative evolution with the target thickness

Figure 4 presents the evolution of delayed Lyman ($np\rightarrow 1s$) intensities, for different carbon target thickness, as a function of the distance d behind the foil corresponding to delay times longer than 20 ps. For the sake of clarity, we normalized all data to the case of a 3.5 $\mu g/cm^2$ target at a distance $d=1.05$ mm (i.e., $t\approx 20$ ps).

As found by several authors [4,20,21], the evolution of experimental photon intensities $\tilde{N}_{X/ion}^{np}(t)$ with t is well repre-

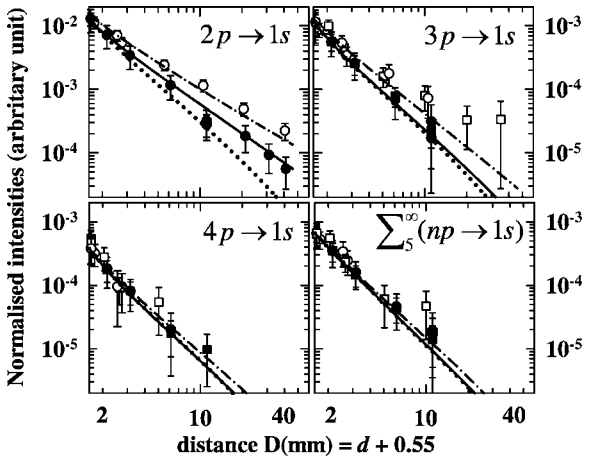

FIG. 4. Normalized evolution of the Lyman line emission (see text) as a function of the distance behind the target: experimental data (symbols: ●, target of 3.5 μg/cm^2, ■, 8.6 μg/cm^2, □, 98 μg/cm^2, and ○, 201 μg/cm^2), binary ion-atom conditions, i.e., including cascade contribution without any transport effects accounted for (dotted curves), classical transport with wake off (solid curves, target of 3.5 μg/cm^2; dash-dotted curves, 201 μg/cm^2). The real distance d behind the target has been arbitrarily shifted by 0.55 mm to clarify the graph.

sented by a power law $\tilde{N}^{np}_{X/ion}(t) \propto t^{-a_{np}}$, where a_{np} is the decay slope of a given state. In these previous studies, performed for one single target thickness, it was observed that $a_{2p} < a_{3p}$. In the present work, decay slopes of $n=2$, 3, 4 and $\Sigma_5^{\infty}(np \rightarrow 1s)$ are measured for a large range of target thickness—from single-collision condition to equilibrium. We found $a_{2p} < a_{3p} < a_{4p} \approx a_{np\ (n>4)}$ for the whole range of target thickness. This result simply accounts for cascade effects. Indeed, the cascade contribution decreases when the principal quantum number n increases, as shown in Table I, and the fewer cascades contribute to the np-state population, the faster the decay.

Regarding now the $2p$ and $3p$ slope dependence on target thickness (i.e., on the number of collisions the projectile ion undergoes), departure of the experimental data from a binary ion-atom collision proves the sensitivity to transport effects. In particular, we found $a_{2p}=1.69\pm0.13$ at $\delta=3.5$ μg/cm^2 and $a_{2p}=1.26\pm0.08$ at $\delta=201$ μg/cm^2. The thickness dependence is smaller for $3p$. For the $np \rightarrow 1s$ transitions with $n \geqslant 4$, the a_{np} values are constant within the error bars ($a_{4p}=2.22\pm0.25$ and $a_{np(n>4)}=1.88\pm0.17$), and no deviation from a binary ion-atom collision is observed. The observed decrease of the a_{2p} slope with target thickness shows evidence for high-ℓ Rydberg-state population values, which develop during ion transport. In addition, as presented Fig. 5, the evolution of a_{2p} and a_{3p} slopes versus foil thickness is well fitted by a decay law $a_{np}=a_{np}^{sat}+a_0 \exp(-\delta/\delta_l)$ with a typical thickness δ_ℓ of 6 μg/cm^2 ($\pm 30\%$). This shows that a stationary regime is reached quite rapidly at approximately 20 μg/cm^2. In other words, equilibrium in high-ℓ Rydberg-state population is established quickly, after typically six collisions (i.e., ion transit time in the solid of 2 fs).

Finally, Figs. 4 and 5 show that classical transport simulations involving multiple scattering are in close agreement

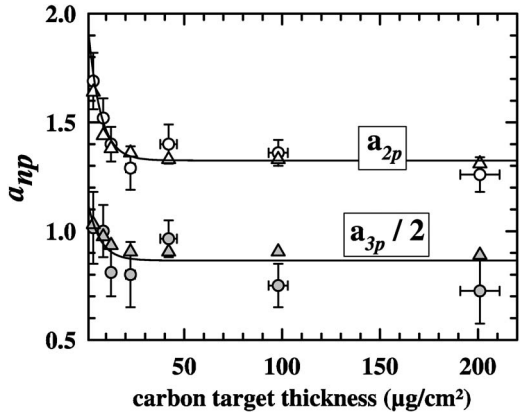

FIG. 5. Slope evolution of the delayed Lyman line intensities versus foil thickness: experiment (symbols with error bars); classical transport (triangles); fit with a decay function given in the text (solid lines). a_{3p} has been divided by 2 to clarify the graph.

with experimental data. Note that only the wake-off predictions are plotted, since, as we shall see below, the slopes are rather insensitive to the inclusion of the wake in the calculation.

2. Absolute Lyman line behavior with ion time of flight (t)

Figures 6–10 present the absolute photon intensities $\tilde{N}^{np}_{X/ion}(t)$ as a function of the delay t for samples of target

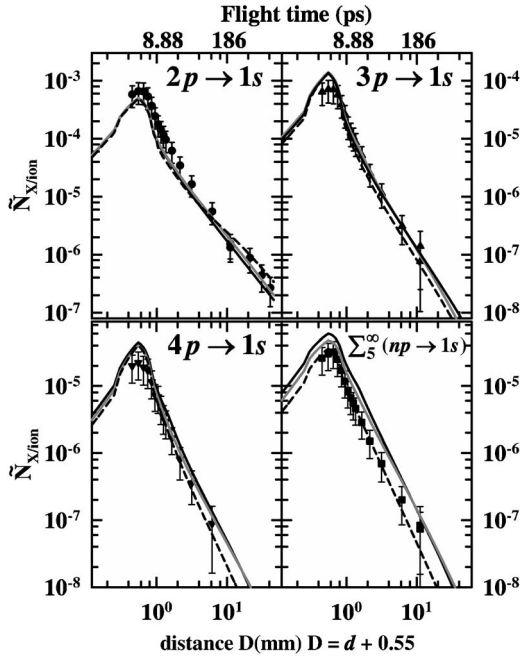

FIG. 6. Evolution with the time of flight of the Ar^{17+} Lyman line intensities (i.e., number of emitted photons per ion) for the 3.5 μg/cm^2 carbon target: experimental results (symbols), classical transport model with wake off (solid black lines) and wake on (solid gray lines), rate-equation model (dashed lines). In the simulations, the CDW calculations have been used to account for the primary capture processes. The distance behind the target has been arbitrarily shifted by 0.55 mm for the sake of clarity.

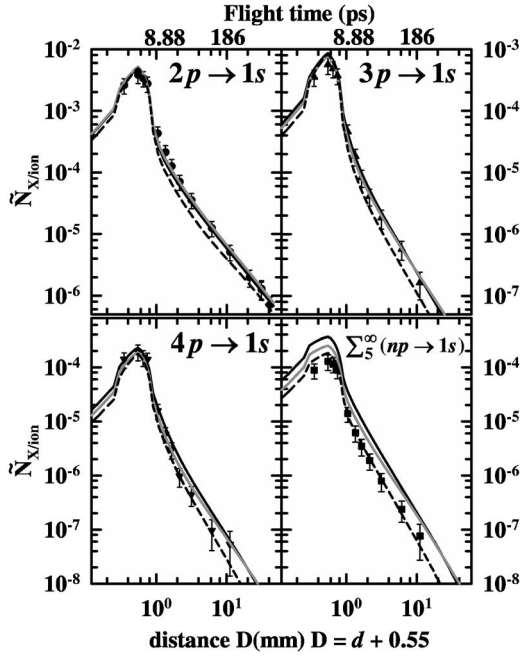

FIG. 7. Same as Fig. 6 for the 8.6 μg/cm^2 target thickness.

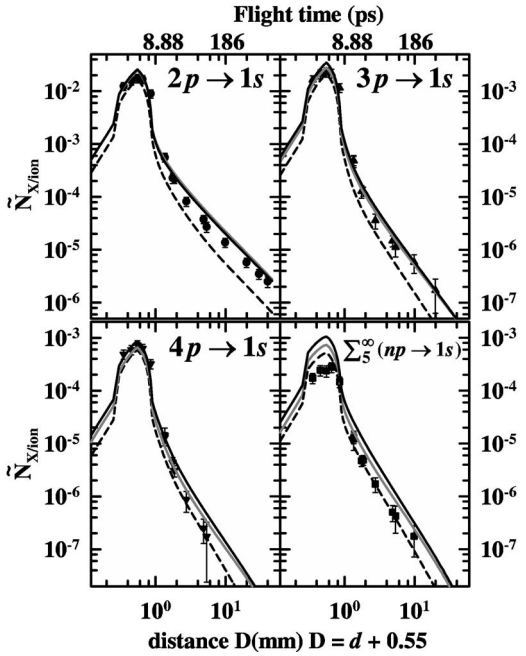

FIG. 9. Same as Fig. 6 for the 42 μg/cm^2 target thickness.

thickness 3.5, 8.6, 12.6, 42, and 98 μg/cm^2. In each figure, the experimental data are compared with the rate-equation model and the classical simulation with or without the wake-field included, respectively, "wake on" and "wake off."

At a first stage, one can see that the three different types of calculation reproduce very well the observed behaviors while comparison addresses to absolute experimental measurements on one side and *ab initio* transport calculations on the other side. A more detailed analysis emphasizes different aspects relevant to weak or strong points of each theoretical approaches. Let us first examine the absolute Lyman line intensities for $t<9$ ps. In this domain of delay times, the shape of the curves is mostly governed by the geometrical effects detailed in the Appendix (obviously affected by the "true" zero position of the target), while the intensity is sensitive to the x-ray autoabsorption. In that respect, for a given thickness, a same average shift of the target has been introduced in the three theoretical approaches. Reasonable values ranging from 5 to 250 μm have been used and allow us to reproduce the evolution of the delayed Lyman lines in the "short" delay time region on an absolute scale. As shown in Figs. 6–10, on the one hand, predictions of the rate-equation

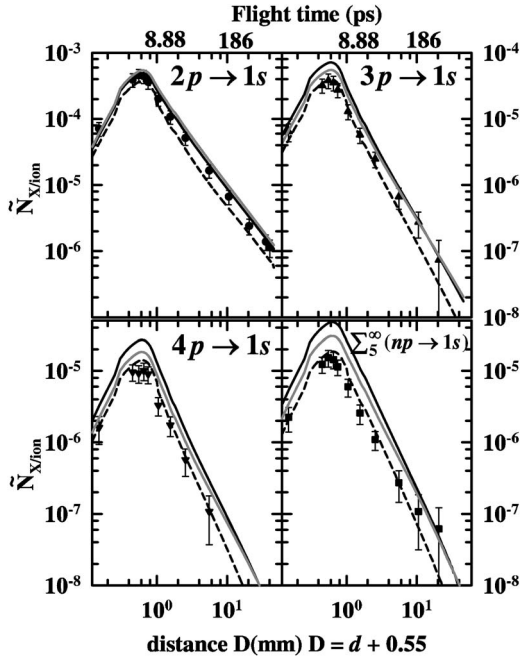

FIG. 8. Same as Fig. 6 for the 12.6 μg/cm^2 target thickness.

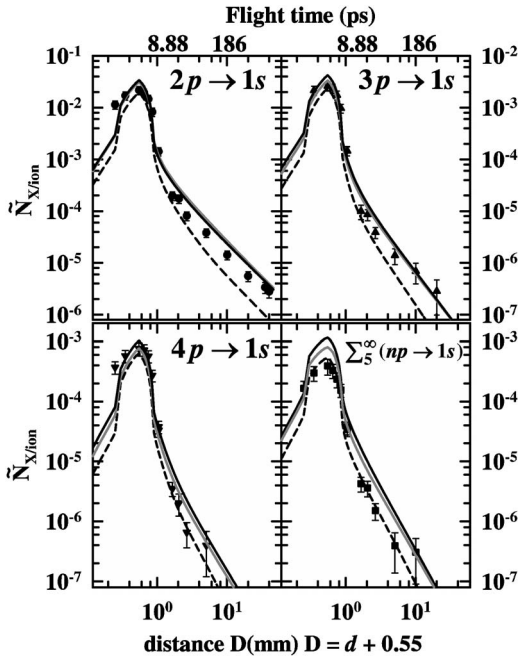

FIG. 10. Same as Fig. 6 for the 98 μg/cm^2 target thickness.

model are in very good agreement with the experimental data whatever the target thickness and for the whole Lyman series. On the other hand, the classical Monte Carlo simulation gives also realistic results, mainly for Lyman α and β lines. The very good agreement obtained with the rate-equation model for short delay is more likely due to the fact that Lyman lines correspond to prompt deexcitation of p states coming mostly from low-n manifolds. In other words, the evolution of the Lyman line intensities, in this restricted delay time domain, is not connected (and therefore not sensitive) to the Rydberg-state population. Considering now the long delay times (i.e., $t>9$ ps), where neither the geometrical effects nor the x-ray autoabsorption play any role, and, looking first at the evolution of Lyman-α and β line intensities, one can see in Figs. 6–10 that the rate-equation model provides also very good predictions for targets thinner than 12.6 $\mu g/cm^2$. Indeed, for thicker targets, this model leads to an underestimation of delayed Ly-α and -β intensities, in particular for long delay. This discrepancy could be ascribed to the empirical treatment used to include the contribution of excited states with $10<n\leqslant 30$ (see Sec. III A), but may also be addressed to the neglected intershell excitation processes with $\Delta n>\pm 1$ for $n>6$, which play a role for thick targets and become as high as those with $\Delta n=\pm 1$ for levels of high n value. For long delay times, the classical transport model with wake off gives very good predictions over the whole range of target thickness for the Lyman-β lines and slightly overestimates the delayed Ly-α line intensities for target thickness higher than 42 $\mu g/cm^2$. Finally, over the whole range of target thickness and delay times, the Ly-γ and $\Sigma_5^{\infty}(np\rightarrow 1s)$ results are better predicted by the rate-equation model than by its classical counterpart, which gives systematically higher values. For these states, the cascades come mainly from upper levels of low ℓ values and their contribution remains small compared to direct population (see Table I). These lines are thus more sensitive to the evolution of inner-shell populations and a quantum treatment, like the rate-equation model, is more suitable than a classical description.

To complete this detailed analysis, the influence of the wakefield on Rydberg-state populations has been examined within the classical Monte Carlo transport approach. As reported in Figs. 6–10, the comparison of the classical simulation with or without wake does not exhibit large differences. In particular, the shape of the curve for long delay remains unaffected and the slopes are similar. Regarding the curve behavior, the observed differences between both simulations are too small to be conclusive in spite of good statistics (statistical uncertainty in the simulation is lower than 2% at 3.5 $\mu g/cm^2$ and lower than 12% at 98 $\mu g/cm^2$).

From this series of comparisons, we conclude that the rate-equation model combined with an empirical inclusion of states with n above 10 is quite robust to reproduce the whole of experimental variations. The classical simulation is obviously much better suited to reproduce the long-delayed Lyman intensities originated from high-ℓ Rydberg states, even though it is less appropriate for the description of internal states, which provides the bulk of the contribution in the Lyman emission. In particular, the classical simulation enables us to quantify the number of contributing highly excited Rydberg states in the long-delayed Lyman intensities [16]. Furthermore, within this approach, a weak sensitivity of the delayed Lyman intensity to the wakefield is found, at least for the system considered here.

B. The 2s-state population

Figure 11 shows the evolution of the $2s_{1/2}$-state population with the carbon target thickness. Since the cascade contribution, coming only from the decay of $\ell=1$ excited states with $n\geqslant 3$, is rather small (see Table I), the evolution of this deeply bound s state gives a direct insight of a pure core-state population during the transport. As in the case of Rydberg states, departure of the experimental data from a binary ion-atom collision (dotted line in Fig. 11) revealed a great sensitivity to transport effects. Simulations including only multiple scattering on the one hand (i.e., the rate-equation model and the classical transport model with wake off) and accounting for both multiple scattering and the wakefield influence on the other hand (i.e., the master-equation model and the classical transport model with wake on) are also reported in Fig. 11.

When comparing with simulations including only multiple scattering (black lines in Fig. 11), one can remark that the experimental 2s population departs from binary collisions much faster than predicted even though the general trend is quite well reproduced. Note that in this case, the classical transport approach gives similar results than the rate-equation model up to a target thickness of around 20 $\mu g/cm^2$. From that point, the rate-equation model saturates more rapidly to achieve a 40% lower population for the

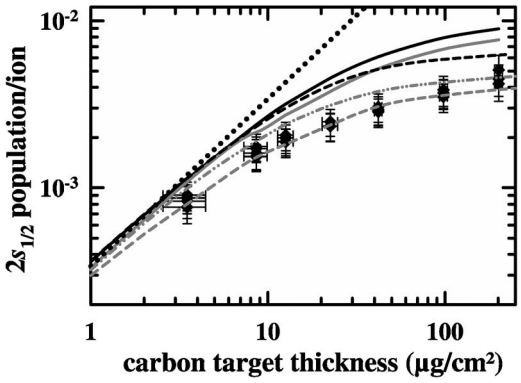

FIG. 11. Absolute $2s_{1/2}$ populations of Ar^{17+} at $v_p=23$ a.u. impact velocity as a function of carbon target thickness: experimental data (symbols); binary ion-atom conditions, i.e., including cascade contribution without any transport effects accounted for (dotted black curve); classical transport model with wake off (solid black line) and wake on (solid gray line); rate-equation model (dashed black line); master-equation model with complete CDW calculations to describe the initial capture process (dashed gray line); and master-equation model with CDW calculations and with the phases of coherences of the initial states taken equal to zero (dash-dot-dotted gray line).

thickest target. To explain this difference between the two approaches, one may examine the effect of the recapture process, which corresponds to the capture of an ionized electron by the ion. This recapture process is accounted for in the classical approach and not in the quantum treatment (in the rate-equation model, ionized electrons are lost). Nevertheless, the evaluation of this process leads to a maximum difference of 20% in the capture population of highly excited states and is far from explaining the extra factor of the classical approach compared to the rate-equation model for the $2s$ population, keeping in mind that the cascade contribution is there very small. Also, this discrepancy between both transport simulations is very probably due to some limitations in the classical treatment of the $2s$ state since it can be shown numerically [34] that classical simulation is not well suited to describe s-state transport in the presence of a Coulomb field, while it leads to better results for p states.

The experimental evolution of the $2s_{1/2}$ population may be explained by the wakefield influence. In fact, this dynamical screening acts directly on the excited levels of the projectile and induces, in particular, binding energy shifts as well as *mixing* of $n\ell j$ substates by the Stark effect [9]. For our system, a substantial $2s_{1/2}$-$2p_{1/2}$ mixing can occur due to both the small Lamb shift in Ar^{17+} (0.158 eV) and the small difference in radiative widths (0.043 eV) compared to the Stark coupling element (0.49 eV). Such ℓ mixing is strongly supported by the fact that only a huge enhancement of intrashell mixing cross sections in the rate-equation model would be able to account for the observed effect on the prompt Lyman lines [16]. As reported in Fig. 11, this effect (see gray lines) plays a much stronger role within the quantum calculation (i.e., the master-equation approach), but has a smaller impact in the case of the classical transport. Besides the limitation in the classical treatment, already discussed above, regarding the description of the s-state transport, any sensibility to the wakefield means that the coherences of the initial sates may play a role and they cannot be taken properly into account in a classical simulation. As can be seen in Fig. 11, if the initial coherences are arbitrarily set equal to zero in the master-equation approach, a perfect matching with the classical treatment is reached but only for very thin targets and large differences between these two simulations occur during the transport (see dash-dot-dotted and full gray lines in Fig. 11). Finally, a proper accounting for CDW phases in the master-equation approach leads hence to a perfect agreement with the experiment (dashed gray line).

V. CONCLUSION AND PERSPECTIVE

A complete study on the production and transport of long-lifetime excited states has been done from the single-collision condition to equilibrium. Using the x-ray spectroscopy technique, evolution of the population of Ar^{17+} ($v_p = 23$ a.u.) Rydberg and $2s$ metastable states has been determined over a large range of carbon thickness. Special attention has been taken to extract absolute cross sections for x-ray production per incident ion of the Rydberg-state decays and for the $2s$-state population. The collision system chosen enables to apply a classical simulation of projectile electron trajectories even for inner shells. Therefore, the whole experimental results can be compared with the predictions of two different transport simulations developed either on a quantum or on a classical phase space. Using the continuum distorted-wave approximation for modeling the initial capture process, both theoretical treatments account for transport effects through the multiple-scattering contributions and the wakefield influence.

The observed decrease of delayed Lyman line intensities (from $2p$, $3p$, $4p$, and $\Sigma_5^\infty np$ to the ground state $1s$) with the ion time of flight t behind the target is well fitted by a power law characterized by decay slopes a_{np}. In particular, the evolution of the a_{2p} slope as a function of the target thickness shows evidence of a strong population in high-ℓ Rydberg states, which develops during the transport and not just at the exit of the foil as claimed previously. Moreover, we have shown that equilibrium in such a Rydberg state population is established very quickly, starting from an ion transit time in the solid of 2 fs. The behavior of absolute photon intensities $\tilde{N}_{Xlion}^{np}(t)$ with the delay t is reasonably well reproduced by the *ab initio* transport calculations we have developed (i.e., the rate-equation model and the classical simulation). Comparisons with theory demonstrate that the evolution of the population of these highly excited states during the transport is mostly governed by multiple scattering. Moreover the classical approach is found to be more suited since $\tilde{N}_{Xlion}^{np}(t)$ has been found to be related to the population of excited states with a principal quantum number n up to $n=30$.

The evolution of the deeply bound $2s$-state population with the target thickness, i.e., the ion transit time, is found also to be very sensitive to transport effects. Nevertheless, contrary to Rydberg states, the models accounting solely for multiple scattering cannot predict correctly the experimental evolution of the $2s$ population even if the general trend is obtained. This evolution exhibits a much stronger and faster $2s$-$2p$ mixing than predicted by collisional mixing. To achieve a complete experimental determination of this particular mixing, the $2p_{1/2}$-state population has to be examined within the same experiment. Recently, we have performed high-precision measurements to determine the evolution of the $2p_j \rightarrow 1s_{1/2}$ transitions as well. Raw comparisons between the gaseous and solid targets show already an enhancement in the population of the $2p_{1/2}$ substate compared to the $2p_{3/2}$ component for solid targets (see Ref. [35] for a complete analysis). This effect is consistent with our present observation on the evolution of the $2s$ population. In addition, the inclusion of the wakefield effect in the transport models improves the predictions leading even to a perfect agreement with the experiment for the quantum treatment. The remaining discrepancy with the classical transport wake-on results is assigned to limitations of a classical treatment in describing transport of deeply bound s states.

The comparisons between absolute measurements and *ab initio* simulations presented here allow us to improve significantly our understanding of ion transport in solids at high velocities.

APPENDIX

The observation of Lyman line intensities with detectors located at 90° with respect to the beam axis and collimated by slits require us to take into account two effects so as to calculate $\tilde{N}^{n\ell}_{X/ion}(t)$ in Eq. (4).

(i) The observed intensity is integrated over Δt since we have used slits of 300 μm width.

(ii) The solid angle is constant when the target is translated along the beam axis but not the geometrical efficiency $\varepsilon_g(Z)$. Indeed, the target holder entails shadow effects when it is in the intercepted region of the detectors.

As mentioned in Sec. II, two cases must be considered to evaluate $\varepsilon_g(Z)$. The first one is the case where the target holder is outside the region intercepted by the collimators. In this case, only delayed Lyman and $2E1$ transitions are recorded. If the target holder is now inside the viewing region, one can still observe delayed Lyman lines but also prompt Lyman lines emitted close to the target. Each type of Lyman transition has to be considered separately. Millimeter units will be used throughout this Appendix.

We first examine the case where the target support is outside the intercepted region by the collimators. $\varepsilon_g(Z)$ is then simply represented by the function depicted in Fig. 12. Then we can easily deduce $\varepsilon_g(Z)$:

$$\varepsilon_g(Z) = \begin{cases} 0, & Z \geqslant 0.87, \\ \dfrac{0.87 - Z}{0.32}, & 0.55 \leqslant Z \leqslant 0.87, \\ 1, & 0.25 \leqslant Z \leqslant 0.55, \\ \dfrac{Z + 0.07}{0.32}, & -0.07 \leqslant Z \leqslant 0.25, \\ 0, & Z \leqslant -0.07. \end{cases}$$

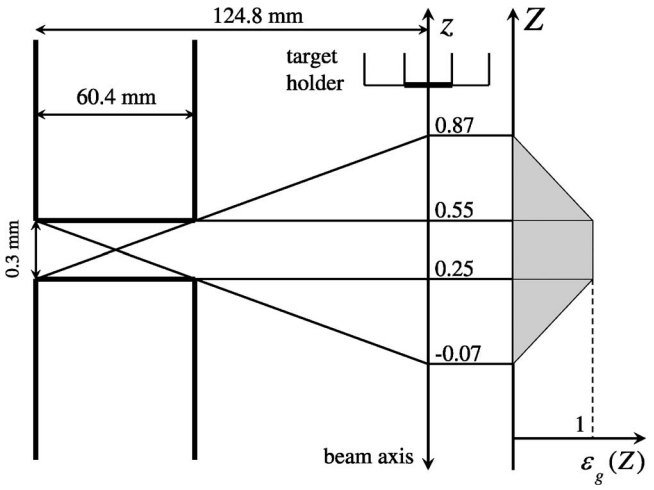

FIG. 12. Geometrical efficiency function of Si(Li) detectors for $z \geqslant 0.87$; z is the position of the target support and Z the position where $n\ell \rightarrow 1s$ transitions are recorded.

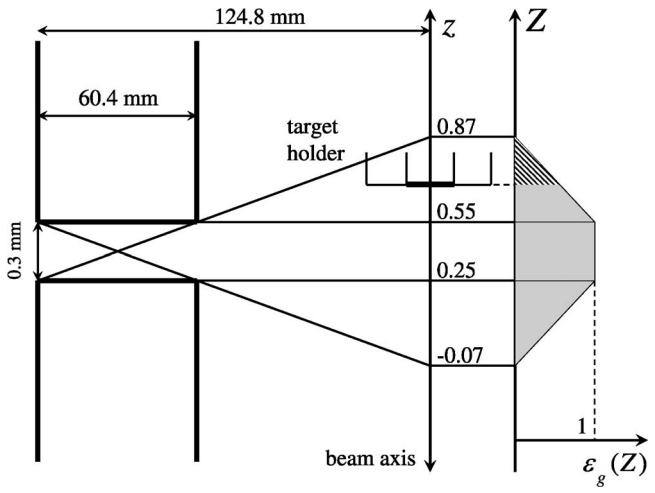

FIG. 13. Same as Fig. 12 for $0.55 \leqslant z \leqslant 0.87$. The hatched area is hidden by the holder.

For short ion times of flight, the target holder is inside the intercepted region (i.e., in our schemes, for $-0.07 \leqslant Z \leqslant 0.87$). This has two effects: the observation area of delayed Lyman lines is reduced and prompt Lyman lines emitted close to the target can now be observed with efficiency depending on the holder position.

For the delayed Lyman lines, three cases have to be considered.

(a) The target position (z) is in the domain $0.55 \leqslant z \leqslant 0.87$ (see Fig. 13). $\varepsilon_g(Z)$ is then given by the same equations as previously but where 0.87 is replaced by z.

(b) The target position is in the interval $0.25 + e \leqslant z \leqslant 0.55$ (see Fig. 14). In this case, the hidden area depends on the holder width, called ℓ. The parameter e is given by

$$e = \frac{0.55 - 0.25}{124.8} \frac{\ell}{2}.$$

Hence, we have

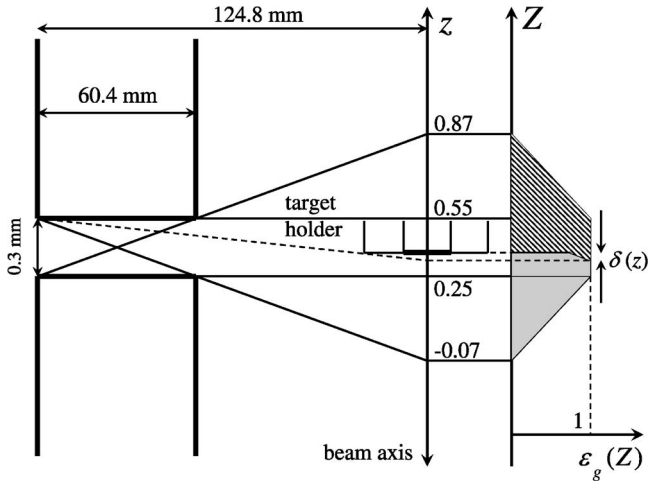

FIG. 14. Same as Fig. 13 for $0.25 + e \leqslant z \leqslant 0.55$. The parameters e and $\delta(z)$ are defined in the text.

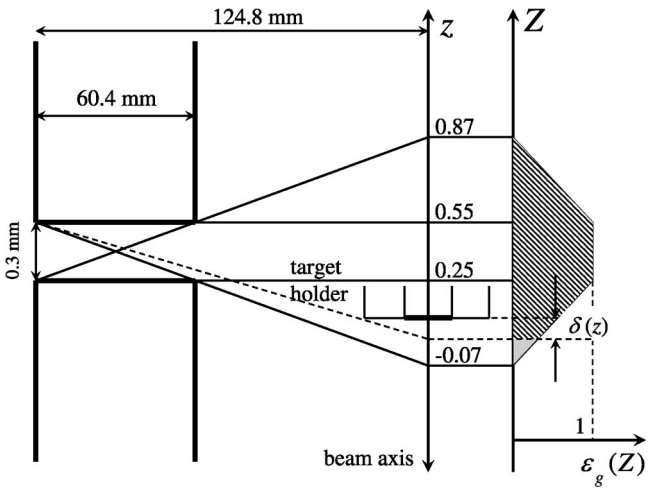

FIG. 15. Same as Fig. 13 for $-0.07+e' \leqslant z \leqslant 0.25+e$. The parameters e, e'; and $\delta(z)$ are defined in the text.

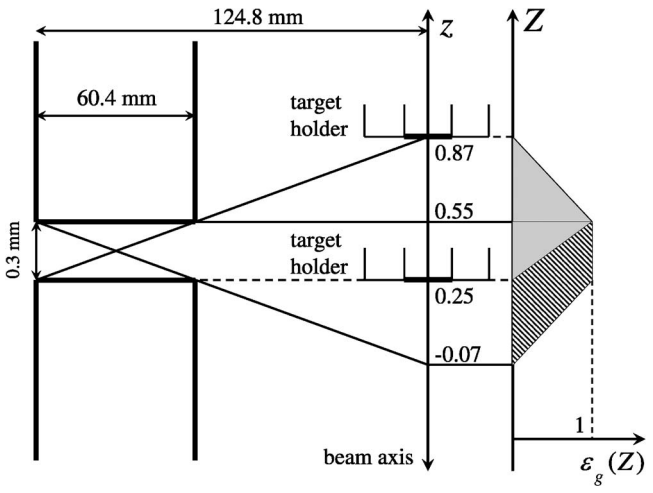

FIG. 16. Same as Fig. 13 for $0.25 \leqslant z \leqslant 0.87$.

$$\varepsilon_g(Z) = \begin{cases} 0, & Z \leqslant -0.07 \text{ or } Z \geqslant z, \\ \dfrac{z-0.25}{0.3} + \dfrac{0.55-z}{0.3\,\delta(z)}(z-Z), & z-\delta(z) \leqslant Z \leqslant z \text{ where} \\ & \delta(z) = \dfrac{0.55-z}{124.8-\ell/2}\dfrac{\ell}{2}, \\ 1, & 0.25 \leqslant Z \leqslant z-\delta(z), \\ \dfrac{Z+0.07}{0.32}, & -0.07 \leqslant Z \leqslant 0.25. \end{cases}$$

(c) The target position is in the interval $-0.07+e' \leqslant z \leqslant 0.25+e$ (see Fig. 15). Here, the parameter e' is given by

$$e' = \frac{0.55+0.07}{124.8}\frac{\ell}{2}$$

Finally, we have

$$\varepsilon_g(Z) = \begin{cases} 0, & Z \leqslant -0.07 \text{ or } Z \geqslant z-\delta(z), \\ \dfrac{Z+0.07}{0.32}, & -0.07 \leqslant Z \leqslant z-\delta(z). \end{cases}$$

In the experimental conditions used here, prompt Lyman lines can be recorded only if $0.25 \leqslant z \leqslant 0.87$ (see Fig. 16). In this case, the geometrical efficiency is only a function of z:

$$\varepsilon_g(Z) = \begin{cases} 0, & z \geqslant 0.87 \quad \text{and } z \leqslant 0.25, \\ \dfrac{z-0.25}{0.30}, & 0.25 \leqslant z \leqslant 0.55, \\ \dfrac{0.87-z}{0.32}, & 0.55 \leqslant z \leqslant 0.87. \end{cases}$$

[1] G. Schiwietz, Nucl. Instrum. Methods Phys. Res. B **175–177**, 1 (2001).
[2] H. D. Betz, D. Röschenthaler, and J. Rothermel, Phys. Rev. Lett. **50**, 34 (1983).
[3] H. D. Betz, J. Rothermel, and D. Röschenthaler, Phys. Rev. A **30**, 1125 (1984).
[4] C. Can, R. J. Maurer, B. Bandong, and R. L. Watson, Phys. Rev. A **35**, 3244 (1987).
[5] J. Kemmler, J. Burgdörfer, and C. O. Reinhold, Phys. Rev. A **44**, 2993 (1991).
[6] J. Burgdörfer and C. Bottcher, Phys. Rev. Lett. **61**, 2917 (1988).
[7] J. Burgdörfer and J. Gibbons, Phys. Rev. A **42**, 1206 (1990).
[8] D. Vernhet, J. P. Rozet, E. Lamour, B. Gervais, and L. Dubé, in *Physics of Electronic and Atomic Collisions*, edited by Y. Itikawa *et al.*, AIP Conf. Proc. **500**, 666 (2000).
[9] J. P. Rozet, D. Vernhet, I. Despiney-Bailly, C. Fourment, and L. Dubé, J. Phys. B **32**, 4677 (1999).
[10] D. Vernhet, C. Fourment, E. Lamour, J. P. Rozet, B. Gervais, L. Dubé, F. Martin, T. Minami, C. O. Reinhold, M. Seliger, and J. Burgdörfer, Phys. Scr., T **92**, 233 (2001).
[11] D. G. Arbó, C. O. Reinhold, P. Kürpick, S. Yoshida, and J. Burgdörfer, Phys. Rev. A **60**, 1091 (1999).
[12] C. O. Reinhold, D. G. Arbo, J. Burgdörfer, B. Gervais, E. Lamour, D. Vernhet, and J. P. Rozet, J. Phys. B **33**, L111 (2000).
[13] T. Minami, C. O. Reinhold, M. Seliger, J. Burgdörfer, C. Fourment, E. Lamour, J. P. Rozet, D. Vernhet, and B. Gervais, Phys. Rev. A **65**, 032901 (2002).
[14] T. Minami, C. O. Reinhold, and J. Burgdörfer, Phys. Rev. A **67**, 022902 (2003).
[15] J. P. Rozet, C. Stephan, and D. Vernhet, Nucl. Instrum. Methods Phys. Res. B **107**, 67 (1996).
[16] D. Vernhet, J. P. Rozet, E. Lamour, B. Gervais, and L. Dubé,

Phys. Scr., T **80**, 83 (1999).
[17] I. Despiney, Ph.D. thesis, Université Paris 6, 1994 (unpublished).
[18] D. Vernhet, J. P. Rozet, I. Despiney-Bailly, C. Stephan, A. Cassimi, J. P. Grandin, and L. Dubé, J. Phys. B **31**, 117 (1998).
[19] C. Fourment, Ph.D. thesis, Université Paris 6, 2000.
[20] J. Rothermel, H. D. Betz, and F. Bell, Nucl. Instrum. Methods Phys. Res. **194**, 341 (1982).
[21] J. Pálinkás, G. J. Pedrazzini, D. A. Church, R. A. Kenefick, C. A. Fulton, R. L. Watson, and D. W. Wang, Phys. Rev. A **31**, 598 (1985).
[22] S. P. Goldman and G. W. F. Drake, Phys. Rev. A **24**, 183 (1981).
[23] P. Indelicato (private communication).
[24] H. W. Koch and J. W. Motz, Rev. Mod. Phys. **31**, 920 (1959).
[25] K. Bernhardi, E. Hang, and K. Wiesmann, At. Data Nucl. Data Tables **28**, 461 (1983).
[26] R. Anholt, C. Stoller, J. D. Molitoris, D. W. Spooner, E. Morenzoni, S. A. Andriamonje, W. E. Meyerhof, H. Bowman, J. S. Xu, Z. Z. Xu, J. O. Rasmussen, and D. H. H. Hoffmann, Phys. Rev. A **33**, 2270 (1986).
[27] Y. Inagaki, K. Shima, and H. Maezawa, Nucl. Instrum. Methods Phys. Res. B **27**, 353 (1987).
[28] T. He, R. P. Gardner, and K. Verghese, Nucl. Instrum. Methods Phys. Res. A **299**, 354 (1990).
[29] Dz. Belkic, R. Gayet, and A. Salin, Phys. Rep. **56**, 279 (1979).
[30] J. Burgdörfer and L. J. Dubé, Phys. Rev. Lett. **52**, 2225 (1984).
[31] P. Nicolaï, M. Chabot, J. P. Rozet, M. F. Politis, A. Chetioui, C. Stephan, A. Touati, D. Vernhet, and K. Wohrer, J. Phys. B **23**, 3609 (1990).
[32] J. Müller and J. Burgdörfer, Phys. Rev. A **41**, 4903 (1990).
[33] J. D. Fuhr, V. H. Ponce, F. J. Garcia de Abajo, and P. M. Echenique, Phys. Rev. B **57**, 9329 (1998).
[34] M. Beuve, B. Gervais, E. Lamour, J. P. Rozet, D. Vernhet, and L. J. Dubé, Phys. Lett. A **274**, 37 (2000).
[35] Seliger *et al.* (unpublished).